

Aromatic Additives Boost the Terahertz Properties of Mixed Halide Perovskite Single Crystals

Sarvani Jowhar Khanam, Srinivasa Rao Konda,* Wei Li,* and Banavoth Murali*



Cite This: *J. Phys. Chem. Lett.* 2023, 14, 5624–5632



Read Online

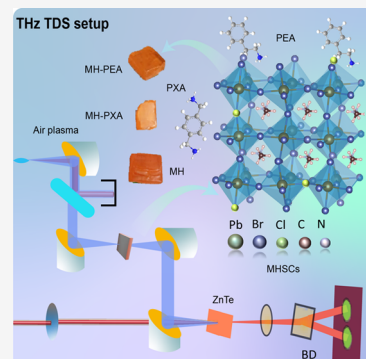
ACCESS |

Metrics & More

Article Recommendations

Supporting Information

ABSTRACT: Mixed halide perovskite (MHP) materials are promising candidates for photonic applications, owing to their tunable bandgap and pronounced optoelectronic properties. However, phase segregation in these materials severely impacts their scalability. The additive engineering (AE) strategy in the growth of most perovskite crystals (PSCs) has proven more effective. Current work focused toward enhancing the stability of 6.67% Cl-doped methylammonium lead(II) bromide single crystals (MHSCs) using aromatic nitrogen-based additives. Modified MHSCs showed enhanced terahertz (THz) radiation transmission and reflection. Moreover, the evidence from powder X-ray diffraction (p-XRD), X-ray photoelectron spectroscopy (XPS), and THz transmission in modified MHSCs revealed the mitigated phase segregation in modified MHSCs.



Mixed halide perovskite single crystals (MHSCs) are auspicious resources in nearly all fields of science and technology, such as light-emitting diodes (LEDs),^{1–5} lasers,^{6,7} memristors,⁸ photovoltaics,^{9–16} photocatalysis,¹⁷ and higher energy radiation detectors.^{18,19} MHSCs are promising materials for future application owing to their tunable bandgap, higher optoelectronic properties, dielectric constant,²⁰ and low-cost processability.²¹ The ABX₃ type of unit cell structure is present in these materials, in which monovalent “A” cations are located in the voids between interlinked octahedra, indirectly affecting the bandgap.^{22–26} The bandgap is formed by combining the metal and halide (MX₆, octahedral unit) s and p orbitals. Changing the concentration of halides/metals can directly affect the bandgap.²⁷ The standard crystallization techniques are antisolvent vapor-assisted crystallization (AVC)^{28,29} and inverse temperature crystallization (ITC).^{30,31}

The potential factors influencing surface quality, crystallinity, and halide segregation depend upon the crystal growth technique,³² the stoichiometry of the concentration/composition,^{33,34} including the solvent,³⁵ the annealing temperature of the precursor,³⁶ and the crystal growth period.³⁷ Cl doping into perovskite precursor solutions has been widely reported to tune the optoelectronic properties of organic–inorganic halide perovskites (OIHPs).^{38,39} Mix et al. investigated different Cl-doping concentrations and reported that increased LED performances in optimized MHSCs outperformed their counterpart in optoelectronic properties.³⁸ However, the challenges associated with MHSCs are phase segregation and compositional instability under ambient conditions, which are yet to be explored more in MHSCs.^{38,39} The phase segregation effect is well-described in microcrystalline thin films.^{40,41}

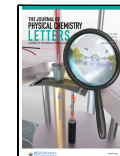
During this process, the perovskite demises into regions of differing halide content, adversely affecting the optoelectronic properties by acting as traps, limiting the prospects of MHSC technology.⁴² Hence, decreasing/increasing the Cl concentration in MHSCs is anomalous and distinctly different from the monotonic growth trend reported in Br/Cl double-halide alloys, which depends upon the nature of molecular bonds on the surface.^{42–44} Nevertheless, limited reported techniques are available on the additives engineering for three-dimensional (3D) MHSCs in the literature to mitigate phase segregation.^{42–44} Herein, in this work, we optimized 6.67% Cl-doped MHSCs to study the effect of aromatic additives on structural and optical properties of MHSCs. The aromatic additives used are phenylethylamine hydrochloride (PEA) and *p*-xylylenediamine dihydrochloride (PXA).

Methylammonium bromide (MABr) is a hygroscopic salt; on the surface of the crystals, it absorbs moisture and converts to methylammonium (MA), resulting in lead(II) halide (PbX₂) and halogen gases (X₂) forming a vacant surface on MHSCs, as illustrated in Figure 1a.⁴⁵ The N-based aromatic organic molecules with monoamine and diamine groups are prone to interact more with the inorganic octahedra and are more stable than their MABr counterparts. Each column in panels b–d, e–g, and h–j of Figure 1 represents the chemical structure of

Received: March 9, 2023

Accepted: June 7, 2023

Published: June 13, 2023



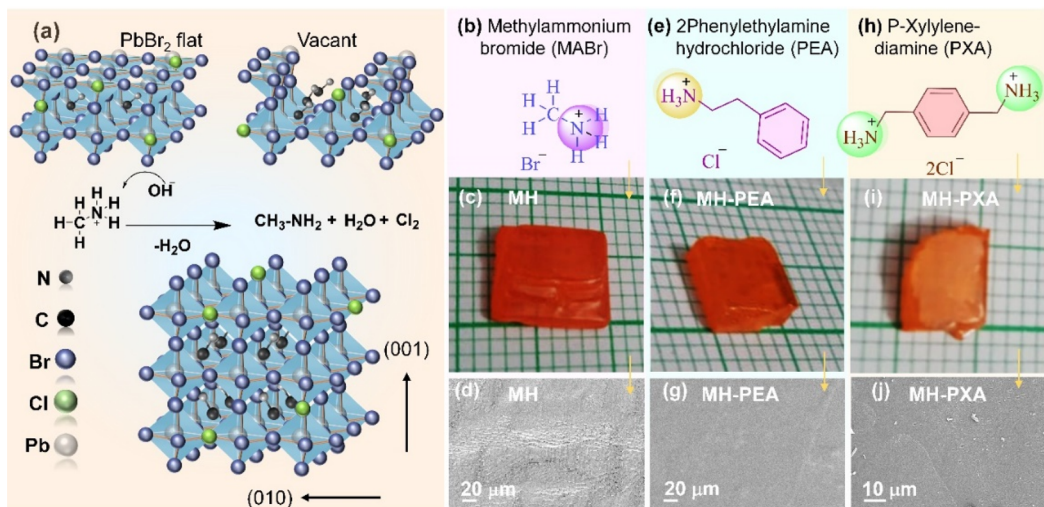


Figure 1. (a) Schematics of surface degradation of MHSCs in the presence of atmospheric moisture and (b–d, e–g, and h–j) each column representing the MABr, PEA, and PXA, chemical structure photographs, and SEM images, respectively.

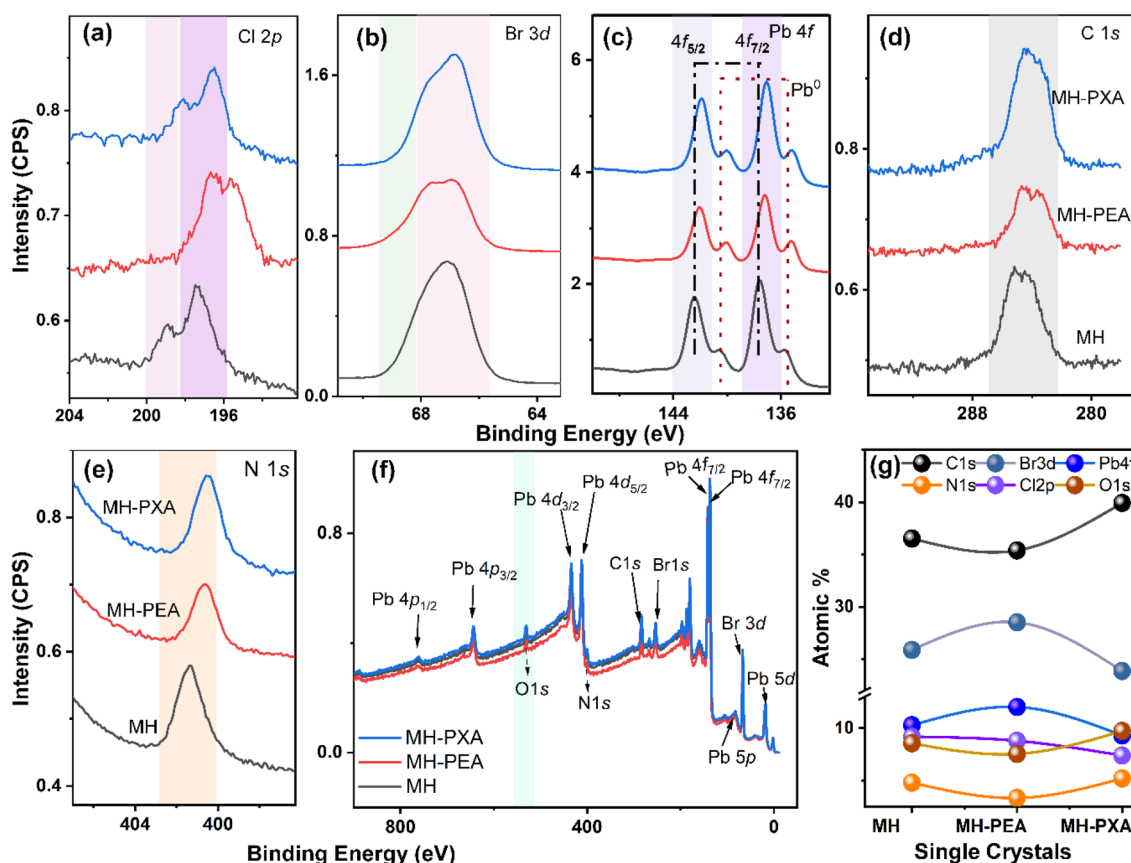


Figure 2. (a–e) XPS data of Cl 2p, Br 3d, Pb 4f, C 1s, and N 1s core-level spectra with molecular level defect and chemical state behavior in MHSCs with changing additives, (f) change in the XPS survey of each SC with different additives, and (g) atomic percent values of each element in reported SCs.

MABr, PEA, and PXA, grown crystal images, and changing crystal surface recorded using scanning electron microscopy (SEM), respectively. Interestingly, we observed flat surfaces with more transparency and low surface roughness in modified MHSCs, suggesting the reduced surface trap states, owing to the effective bonding interaction with additives on the surface,⁴⁶ with weight percent values of modified and pristine MHSCs (Figure S2 of the Supporting Information) and

elemental ratios extracted from the energy-dispersive X-ray (EDX) data (Table S1 of the Supporting Information).

X-ray photoelectron spectroscopy (XPS) studies have been conducted to predict the change in the chemical state behavior of core-level orbitals with additives. A considerable shift in Cl 3d and Br 3d core-level spectra toward lower energies was observed in MH-PXA and MH-PEA SCs, indicating the decreased binding energy resulting from increased halide

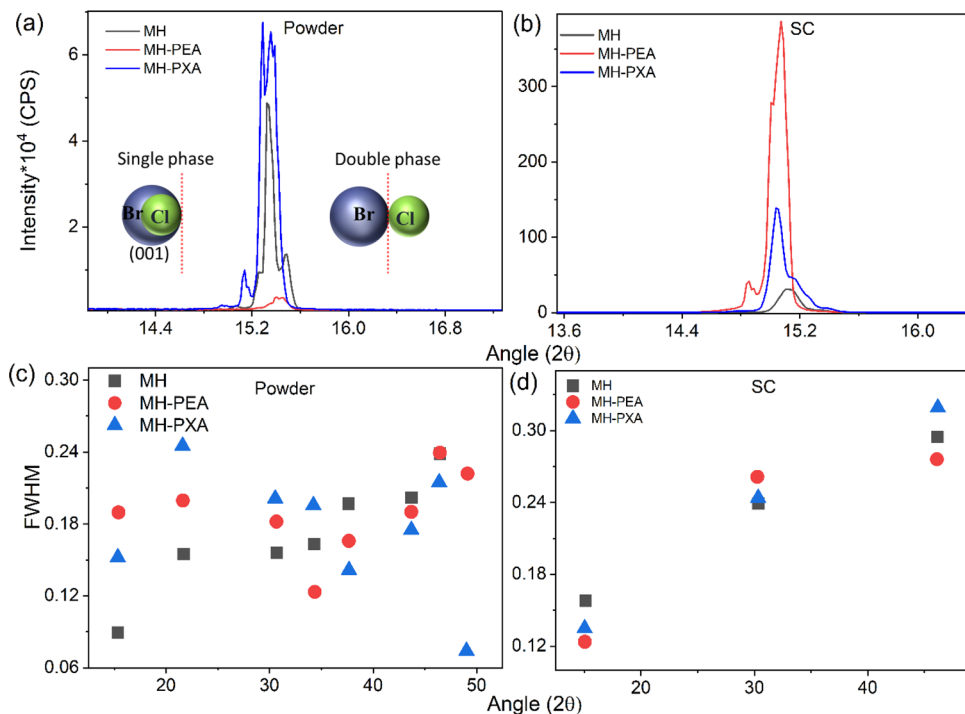


Figure 3. XRD pattern of the modified and pristine SCs: (a and b) splitting and shifting of powder and single-crystal (SC) p-XRD, with (100) peaks showing the transition from single-phase MHSCs to double-phase segregation with different additives, and (c and d) change in fwhm for powder and single-crystal MHSC p-XRD peaks.

vacancies (panels a and b of Figure 2).⁴⁷ Interestingly, intensities of the additional peak in Pb 4f, C1s, and N 1s core-level binding relating to a residual molecule Pb⁰ and CH₃NH₂ have decreased in modified crystals compared to pristine crystals (panels c–e of Figure 2). However, more intense molecular defects and Pb⁰ peaks were seen in the PXA-modified crystals. The XPS survey and changes in the atomic percentages (%) of halides for MHSCs with additives are illustrated in panels f and g of Figure 2. The Cl/Pb ratio of the SC surface also increased when a higher fraction of Cl was injected into the precursor solution.

Further, powder X-ray diffraction (p-XRD) was conducted to verify the effect of additives on lattice parameters and diffraction angles (2θ values) for powder and SC samples. The pristine Bravais lattice MHSCs corresponding to (100), (200), and (300) planes comply with the previously reported data (Figure S3 of the Supporting Information).^{38,48} Generally, replacing Br⁻ with Cl⁻ in the perovskite lattice fosters the unit structure to expand as a result of the confinement effect caused by decreased Pb–X distances. Meanwhile, if the peak shift is toward higher angles, the host unit cell structure is contracting and vice versa. From Figure 3b, we could observe the diffraction peak of MHSCs toward the smaller diffraction angle after using the additives, indicating lattice expansion depending upon the Cl concentration. As in MH-PEA, the bandgap evolution inflection point (or the phase boundary between the single-phase double-halide alloy and phase segregation) consistently increased with an increased N content. Panels c and d of Figure 3 indicate a more comprehensive single-phase range full width half maximum (FWHM) and greater tolerance to phase segregation in the perovskite with a higher Br content than that of MH-PXA with a higher Cl content.⁴⁹ Subsequently, the microstrain values have been calculated from p-XRD data using Williamson–Hall (W–H) plots, at

8.436×10^{-4} , 8.140×10^{-4} , and 0.950 for MH, MH-PEA, and MH-PXA, respectively (panels a–c of Figure S4 of the Supporting Information).⁵⁰ A higher lattice strain is observed in the case of MH-PXA with more FWHM and peak splitting, which might be due to increased intrinsic defects as a result of halide segregation on the surface of PSCs. XPS data also strengthened the argument of increased intrinsic defects by decreasing the photoemission energy. However, structural evolution observed with XRD reveals that the bandgap decrease at a high Cl content was caused by phase segregation into two perovskite phases (inset in Figure 3a). Trends obtained in XRD peaks are consistent with the elemental ratios calculated using the XPS atomic percent and suggest the segregation of a high Br/Cl phase, which left behind a Br-rich surface.

Furthermore, high-resolution transmission electron microscopy (HRTEM) measurements have been performed to check the changes in the selected area electron diffraction (SAED) pattern by changing additives.^{51–54} HRTEM images, lattice fringes, and SAED have been recorded (panels a–c, d–f, and g–i of Figure 4). The bright lattice fringes of modified MHSCs in HRTEM images depicted lattice plane distances (d space) of 0.216, 0.345, and 0.250, corresponding to (220), (111), and (200) planes, respectively. SAED patterns exhibit a well-defined crystalline nature of modified MHSCs. Consequently, for all MHSCs, the calculated lattice constant from transmission electron microscopy (TEM) images (using GATAN software) is very close to the estimated value from p-XRD using the Bragg diffraction equation. The collected TEM images were taken by selecting a spot from different locations on the grid because perovskite materials are volatile in high-energy electron beams. Hence, analyzing the element distribution for long-time electron beam exposure is challenging.

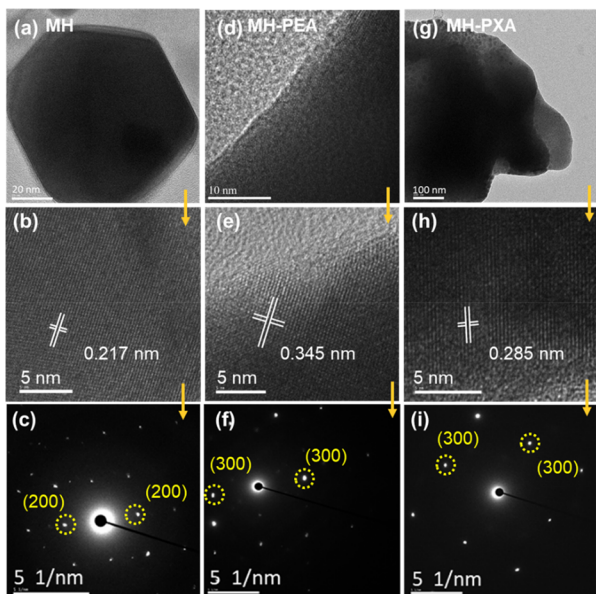


Figure 4. (a–c, d–f, and g–i) TEM images, HRTEM images with lattice fringes, and SAED of each MH, MH–PEA, and MH–PXA SC, respectively.

In general, replacing Br^- with Cl^- in the perovskite lattice increases the bandgap of materials, which is attributed to the downshift of the valence band maximum (VBM) (increased electronegativity) and the upward shift of the conduction band minimum (CBM) (increase in ionization energy). The decrease in $\text{Pb}-\text{X}$ distances causes the confinement effect; both the electronegativity effect and the confinement effect of the halides eventually increase the bandgap. Hence, the MH–PXA SC has more bandgaps than other modified MHSCs. Bandgap values of pristine MHSC are in congruence with previous reports.^{38,39} As discussed in XPS measurements, a

0.112 eV increase in Pb^{2+} orbital binding energy was attributed to the reduced halide vacancies in MH–PEA SCs over the pristine SCs. Considering both the contributions of surface defects toward photoinstability and optimized Cl ratio, this assumed that photoinduced phase segregation reduced in the case of MH–PEA. Optical studies have been carried out to further validate the generality of the defect-free surface on modified MHSCs and to investigate the impact of additives on the bandgap. Ultraviolet–visible (UV–vis) spectroscopic measurements were performed in diffuse reflectance spectra (DRS) mode (Figure 5a), and the bandgap was calculated on the basis of the empirical Kubelka–Munk function (Figure 5b). A slight decrement and increment of 0.002 and 0.003 eV have been observed in MH–PEA and MH–PXA SCs.

The light-induced phase segregation of modified MHSCs was compared to the pristine photoluminescence (PL) measurements recorded under a 800 nm laser (two-photon absorption) in ambient conditions (Figure 5c). This two-photon absorption spectroscopy gives details of the bulk materials. A PL blue shift of modified MHSCs at a high Cl concentration level strongly suggests that incorporating Cl into the lattice employs the halide phase segregation pathways, indicating the increase in non-radiative recombination (induced by deep traps Pb^0 , MA, etc.).^{55,56} The order of PL emission intensity for SCs follows MH > MH–PEA > MH–PXA. The PL intensity shows quadratic dependence up to the 50 mW laser power; after that, it shows the saturation for all samples. Ganeev et al. showed a similar dependence of PL emission from MAPbBr_3 thin films.⁵⁷ This order is more visible after crossing the 50 mW laser power. It represents the photostability of modified MHSCs at different laser powers, forming the more halide-concentrated domains at high-intensity lasers. The XPS and PL data suggested a combination of mechanisms: suppression of the non-radiative recombination, thereby increasing/decreasing the stability/defect states on the surface depending upon the bonding interactions of

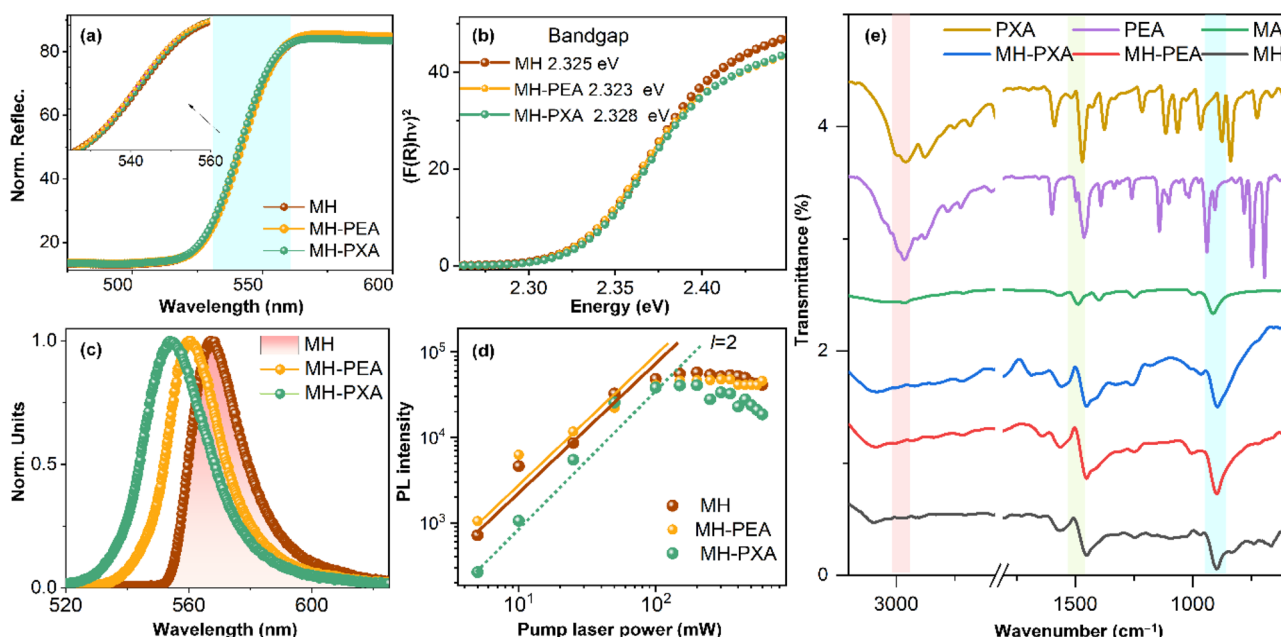


Figure 5. (a) UV–vis spectra, with the enlarged view in the inset, (b) energy versus $F(R(h\nu))^2$ plot, with the MH, MH–PEA, and MH–PXA SCs photoexcited at 800 nm, and the corresponding (c) PL spectra, (d) PL intensity versus input laser power, and (e) FTIR spectra, showing vibrational modes with respect to additives in the modified MHSCs.

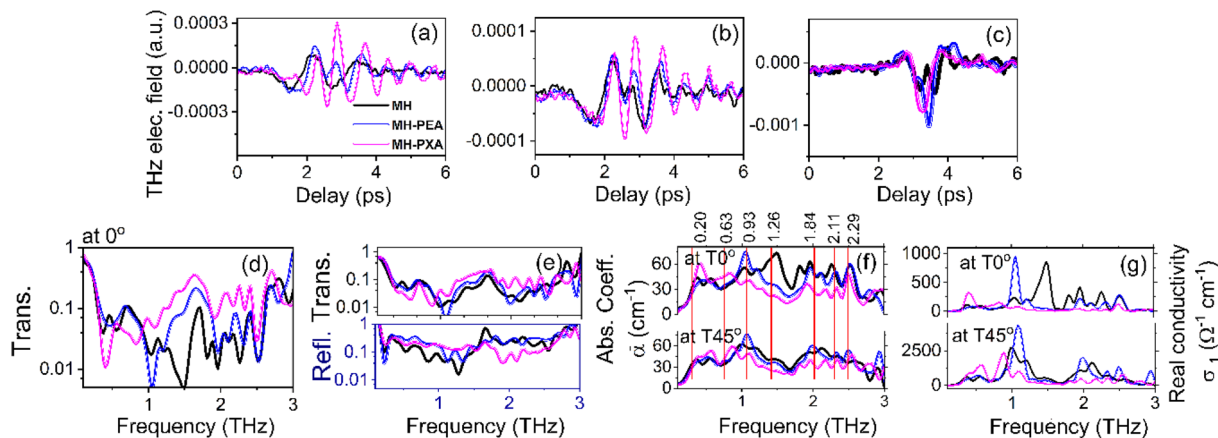


Figure 6. THz electric field of the THz pulse: transmission from MH, MH-PEA, and MH-PXA SCs at (a) 0° and (b) 45° and (c) reflection at 45° with respect to the delay (ps) and transmittance of MH, MH-PEA, and MH-PXA SCs (d) at 0°, (e) transmittance/reflectance at 45°, (f) absorption coefficients, and (g) real conductivity at 0° and 45°, measured relative to the frequency (THz).

additives, and an increase in the intrinsic defect concentration concluded from structural and optical properties. The trends in the lattice constant and bandgap were consistent; in all cases, the bandgap raising rate was ~ 0.002 eV, with each percentage of Cl alloyed.^{38,39,58} Fourier transform infrared (FTIR) spectroscopy generally confirms the presence of additives using the functional group vibrational mode strength in the spectrum and change in the vibrational modes.⁵⁹ The FTIR spectrum of the pristine MHSC showed major shifts of the prominent peaks at 894, 1245, 1451, and 3097 cm^{-1} , which are attributed to the C–N stretch (ν_5), sym-NH $_3^+$ bend (ν_3), asym-NH $_3^+$ bend (ν_9), and sym-NH $_3^+$ stretch (ν_1), respectively. This peak shifted by adding the additives owing to changes in the MA $^+$ interaction with the Pb–X inorganic octahedron. The N–H stretch trend should increase (band position increases) for the Cl concentration because it is more electronegative than bromide. In the spectra of the modified MHSCs, the characteristic peaks of the unsaturated benzene C–H vibrational mode in the region of 3005 cm^{-1} are visible in the modified MHSC spectrum, indicating the presence of aromatic additives on the surface, coordinated with the Pb $^{2+}$ ions. The change in vibrational modes with additives in the modified MHSCs from 1000 to 600 cm^{-1} is provided in Figure S5 of the Supporting Information.

Terahertz (THz) studies were conducted in transmittance and reflection modes to justify surface artifacts and to study the crystal depth profile of MHSCs. THz radiation could be generated by focusing femtosecond amplifier pulses of 800 nm and its second harmonic wavelengths (two-color pump) into ambient air, which is one of the potential sources.^{60–65} Several researchers explored the diversity of THz applications in optics, photonics, biomedicine, and imaging.^{66–70} Meanwhile, terahertz time-domain spectroscopy (THz-TDS) has been developed as a promising technique in science and medicine.^{71–74} Earlier, research groups have studied a variety of OIHPs in the THz range.^{75–83} Therefore, THz-TDS is one of the prominent techniques to ascertain the response of a material in terms of transmission and reflection properties and can obtain the absorption coefficient raised as a result of the optical phonon vibrations. In the present study, we measured THz pulse transmission and reflection from MH series PSCs. Figure S1 of the Supporting Information depicts the experimental setup used for THz-TDS. The corresponding transmission of the THz electric field (temporal profile) from

MH, MH-PEA, and MH-PXA was positioned at normal incidence to the reference THz pulse (transmission at 0°) (Figure 6a) and transmission/reflection at 45° (panels b and c of Figure 6) for delay (ps), while at the same time, transmission at 0° (Figure 6d), transmittance/reflectance at 45° (Figure 6e), absorption coefficients (Figure 6f), and real conductivity at 0° and 45° (Figure 6g) were measured with respect to the frequency (THz).

The measured transmittance for PSCs was at 0° (THz amplitude for PSCs/THz amplitude reference pulse) (Figure S6a of the Supporting Information). The reference THz pulse has a bandwidth of up to 3.0 THz, having a maximum peak intensity of around 1 THz. The transmitted/reflected THz pulses have less peak intensity and bandwidth as a result of the absorption of SCs. The SCs possess higher reflection than transmission. Also, for the reflectance (bottom panel of Figure S6b of the Supporting Information); the additive SCs are much superior to transmittance (upper panel of Figure S6b of the Supporting Information) compared to pristine SCs. The transmission at 45° is lower than 0° as a result of the extended path length because the orientation of MHSC at 45° increases the interacting length of THz pulses. It is familiar that, on the basis of the transmission data of THz pulses from SCs, one can obtain the absorption coefficient and conductivity by knowing the real/imaginary parts of the refractive index. The equations used for these measurements were reported elsewhere.^{84–89} Here, the thickness of the PSCs plays a key role in these measurements. The measured thickness of MH, MH-PEA, and MH-PXA, using digital vernier calipers, is followed by 1.45, 1.44, and 1.47 mm, respectively. The measured absorption coefficients and real conductivity of SCs are at T0° and T45° (panels g and h of Figure 6), respectively. The peak position absorption and conductivity for each SC are almost identical, except for the 1.5 THz for MH.

Meanwhile, it is observed that the modified MHSCs shift in their absorption/conductivity peaks compared to those of the pure MH crystal; this might be due to a change in the morphology and chemical composition of additive-based MHSCs. Earlier, three phonon modes (0.8, 1.4, and 2.0 THz) associated with pure MAPbBr₃ SCs were determined by Maeng et al.⁴⁷ using first-principles simulations. The Pb–Br–Pb bonds show transverse and longitudinal optical vibrations at 0.8 and 1.4 THz, respectively, whereas 2.0 THz corresponds to the optical Br vibration. However, other vibrational frequencies

are present in the optical infrared (IR) vibrational spectra reported by Maeng et al.⁴⁷ Those frequencies are labeled as solid red lines, and the corresponding values are shown on the top axis of Figure 6g. Earlier, the vibrational modes of MAPbX₃ (X = Cl, Br, and I) using Raman spectroscopy and theoretical simulations were demonstrated by Brivio et al.⁸⁹ Chlorine-contained PSCs have higher vibrational frequencies than the bromide- and iodine-based SCs.⁹⁰ In the present case, we have grown the MHSCs in different additives (PEA and PXA). Therefore, these additives contributed to the weight and atomic percent changes in modified MHSCs compared to the pristine SCs (C, N, Pb, Br, and Cl) confirmed by XPS data. As a result, the vibrational frequencies depend upon the chemical bonding between Pb–Br/Cl–Pb and individual Br and Cl optical vibrations. Hence, the frequencies of the resultant absorption/conduction spectra are shifted in comparison to pure MHSC. Moreover, additive PEA has influenced crystal morphology and enhanced THz transmission and reflection. As a result, the absorption/conductivity becomes weaker, which implies the applicability of additive-based PSCs in the THz range.

In summary, we have successfully demonstrated an AE strategy for mitigating the mixed halide phase segregation effect of 6.67% Cl-doped MHSCs with additives. Of all of the additives that we have observed, a bluer shift in PL emission for MH–PXA SC when excited with a 2PA source laser indicates more non-radiative recombination. Interestingly, we observed increased crystallinity with mitigated phase segregation (concluded from p-XRD and XPS studies). The lattice constant of the PEA–MHSCs is greater than PXA and pristine MHSC, suggesting increased Schottky order and transparency in the bulk perovskite. This explanation is consistent with the increased interaction between the formation of MHSCs, with PEA additives being more thermodynamically preferred than other additives. The present work will open the door for obtaining more transparent flat surface crystals with low trap states for photodetection applications, particularly THz and higher energy radiation detection with excellent resolution.

■ ASSOCIATED CONTENT

① Supporting Information

The Supporting Information is available free of charge at <https://pubs.acs.org/doi/10.1021/acs.jpcllett.3c00649>.

Experimental details of MHSCs, synthesis method, instrumental details (Figure S1), characterization details, EDX weight percent values of modified and pristine MHSCs (Figure S2), elemental ratios extracted from the EDX data (Table S1), p-XRD data, microstrain (Figures S3 and S4), FTIR spectra (Figure S5), THz electric field of the THz amplitude, and phase and frequency spectra (Figure S6) of modified and pristine MHSCs ([PDF](#))

Transparent Peer Review report available ([PDF](#))

■ AUTHOR INFORMATION

Corresponding Authors

Banavoth Murali – Solar Cells and Photonics Research Laboratory, School of Chemistry, University of Hyderabad, Hyderabad, Telangana 500046, India;  orcid.org/0000-0002-7806-2274; Email: murali.banavoth@uohyd.ac.in

Srinivasa Rao Konda – The GPL Photonics Laboratory, State Key Laboratory of Applied Optics, Changchun Institute of Optics, Fine Mechanics and Physics, Chinese Academy of Sciences, Changchun, Jilin 130033, People's Republic of China;  orcid.org/0000-0002-9001-4857; Email: ksrao@ciomp.ac.cn

Sciences, Changchun, Jilin 130033, People's Republic of China;  orcid.org/0000-0002-9001-4857; Email: ksrao@ciomp.ac.cn

Wei Li – The GPL Photonics Laboratory, State Key Laboratory of Applied Optics, Changchun Institute of Optics, Fine Mechanics and Physics, Chinese Academy of Sciences, Changchun, Jilin 130033, People's Republic of China;  orcid.org/0000-0002-2227-9431; Email: weili1@ciomp.ac.cn

Author

Sarvani Jowhar Khanam – Solar Cells and Photonics Research Laboratory, School of Chemistry, University of Hyderabad, Hyderabad, Telangana 500046, India

Complete contact information is available at: <https://pubs.acs.org/10.1021/acs.jpcllett.3c00649>

Author Contributions

Sarvani Jowhar Khanam, conceptualization, data curation, investigation, formal analysis, methodology, and writing—original draft and review and editing; Srinivasa Rao Konda, data curation, investigation, analysis, and writing—original draft and review and editing; Wei Li, resources and writing—review and editing; and Murali Banavoth, funding acquisition, supervision, project administration, formal analysis, methodology, and writing—original draft and review and editing.

Notes

The authors declare no competing financial interest.

■ ACKNOWLEDGMENTS

This work was supported by the School of Chemistry, University of Hyderabad. Banavoth Murali acknowledges the Department of Science and Technology (DST), the Indo-Korea Grant (INT/Korea/P-40), and the Institute of Eminence (UOH-IOE-RC2-21-008). The authors acknowledge the Innovation Grant of Changchun Institute of Optics, Fine Mechanics and Physics (CIOMP), the Jilin Provincial Science and Technology Development Project (YDZJ202102CXJD002), the Development Program of the Science and Technology of Jilin Province (20200802001GH), the Chinese Academy of Sciences President's International Fellowship Initiative (2021PM0036). Srinivasa Rao Konda thanks Rahul A. Rajan, The GPL Photonics Laboratory, for his assistance in collecting the 800 nm PL spectra.

■ REFERENCES

- (1) Diyali, S.; Manna, M.; Mahato, S.; Kumar, V.; Roy Choudhury, A.; Biswas, B.; Bhandari, S. Hybrid Lead Bromide Perovskite Single Crystals Coupled with a Zinc(II) Complex for White Light Emission. *J. Phys. Chem. Lett.* **2022**, *13*, 10759–10766.
- (2) Xiao, Z.; Kerner, R. A.; Zhao, L.; Tran, N. L.; Lee, K. M.; Koh, T. W.; Scholes, G. D.; Rand, B. P. Efficient Perovskite Light-Emitting Diodes Featuring Nanometre-Sized Crystallites. *Nat. Photonics* **2017**, *11*, 108–115.
- (3) Xiao, Z.; Kerner, R. A.; Tran, N.; Zhao, L.; Scholes, G. D.; Rand, B. P. Engineering Perovskite Nanocrystal Surface Termination for Light-Emitting Diodes with External Quantum Efficiency Exceeding 15%. *Adv. Funct. Mater.* **2019**, *29*, 1807284.
- (4) Zhao, L.; Rolston, N.; Lee, K. M.; Zhao, X.; Reyes-Martinez, M. A.; Tran, N. L.; Yeh, Y.; Yao, N.; Scholes, G. D.; Loo, Y.; Selloni, A.; Dauskardt, R. H.; Rand, B. P. Influence of Bulky Organo-Ammonium Halide Additive Choice on the Flexibility and Efficiency of Perovskite Light-Emitting Devices. *Adv. Funct. Mater.* **2018**, *28*, 1802060.

- (5) Zhao, L.; Yeh, Y. W.; Tran, N. L.; Wu, F.; Xiao, Z.; Kerner, R. A.; Lin, Y. L.; Scholes, G. D.; Yao, N.; Rand, B. P. In Situ Preparation of Metal Halide Perovskite Nanocrystal Thin Films for Improved Light-Emitting Devices. *ACS Nano* **2017**, *11*, 3957–3964.
- (6) Xing, G.; Mathews, N.; Lim, S. S.; Yantara, N.; Liu, X.; Sabba, D.; Grätzel, M.; Mhaisalkar, S.; Sum, T. C. Low-Temperature Solution-Processed Wavelength-Tunable Perovskites for Lasing. *Nat. Mater.* **2014**, *13*, 476–480.
- (7) Deschler, F.; Price, M.; Pathak, S.; Klintberg, L. E.; Jarausch, D. D.; Higler, R.; Hüttner, S.; Leijtens, T.; Stranks, S. D.; Snaith, H. J.; Atatüre, M.; Phillips, R. T.; Friend, R. H. High Photoluminescence Efficiency and Optically Pumped Lasing in Solution-Processed Mixed Halide Perovskite Semiconductors. *J. Phys. Chem. Lett.* **2014**, *5*, 1421–1426.
- (8) Xing, J.; Zhao, C.; Zou, Y.; Kong, W.; Yu, Z.; Shan, Y.; Dong, Q.; Zhou, D.; Yu, W.; Guo, C. Modulating the Optical and Electrical Properties of MAPbBr_3 Single Crystals via Voltage Regulation Engineering and Application in Memristors. *Light Sci. Appl.* **2020**, *9*, 11.
- (9) Buriač, J. M.; Kamat, P. V.; Schanze, K. S.; Alivisatos, A. P.; Murphy, C. J.; Schatz, G. C.; Scholes, G. D.; Stang, P. J.; Weiss, P. S. Virtual Issue on Metal-Halide Perovskite Nanocrystals—A Bright Future for Optoelectronics. *Chem. Mater.* **2017**, *29*, 8915–8917.
- (10) Elkins, M. H.; Pensack, R.; Proppe, A. H.; Voznyy, O.; Quan, L. N.; Kelley, S. O.; Sargent, E. H.; Scholes, G. D. Biexciton Resonances Reveal Exciton Localization in Stacked Perovskite Quantum Wells. *J. Phys. Chem. Lett.* **2017**, *8*, 3895–3901.
- (11) Turren-Cruz, S. H.; Hagfeldt, A.; Saliba, M. Methylammonium-Free, High-Performance, and Stable Perovskite Solar Cells on a Planar Architecture. *Science* **2018**, *362*, 449–453.
- (12) Jeong, J.; Kim, M.; Seo, J.; Lu, H.; Ahlawat, P.; Mishra, A.; Yang, Y.; Hope, M. A.; Eickemeyer, F. T.; Kim, M.; Yoon, Y. J.; Choi, I. W.; Darwich, B. P.; Choi, S. J.; Jo, Y.; Lee, J. H.; Walker, B.; Zakeeruddin, S. M.; Emsley, L.; Rothlisberger, U.; Hagfeldt, A.; Kim, D. S.; Grätzel, M.; Kim, J. Y. Pseudo-Halide Anion Engineering for $\alpha\text{-FAPbI}_3$ Perovskite Solar Cells. *Nature* **2021**, *592*, 381–385.
- (13) Jacobsson, T. J.; Hultqvist, A.; García-Fernández, A.; Anand, A.; Al-Ashouri, A.; Hagfeldt, A.; Crovetto, A.; Abate, A.; Ricciardulli, A. G.; Vijayan, A.; Kulkarni, A.; Anderson, A. Y.; Darwich, B. P.; Yang, B.; Coles, B. L.; Perini, C. A. R.; Rehermann, C.; Ramirez, D.; Fairen-Jimenez, D.; Di Girolamo, D.; Jia, D.; Avila, E.; Juarez-Perez, E. J.; Baumann, F.; Mathies, F.; González, G. S. A.; Boschloo, G.; Nasti, G.; Paramasivam, G.; Martínez-Denegri, G.; Nässström, H.; Michaels, H.; Köbler, H.; Wu, H.; Benesperi, I.; Dar, M. I.; Bayrak Pehlivan, I.; Gould, I. E.; Vagott, J. N.; Dagar, J.; Kettle, J.; Yang, J.; Li, J.; Smith, J. A.; Pascual, J.; Jerónimo-Rendón, J. J.; Montoya, J. F.; Correa-Baena, J. P.; Qiu, J.; Wang, J.; Sveinbjörnsson, K.; Hirselandt, K.; Dey, K.; Frohma, K.; Mathies, L.; Castriotta, L. A.; Aldamasy, M. H.; Vasquez-Montoya, M.; Ruiz-Preciado, M. A.; Flatken, M. A.; Khenkin, M. V.; Grischek, M.; Kedia, M.; Saliba, M.; Anaya, M.; Veldhoen, M.; Arora, N.; Shargaeva, O.; Maus, O.; Game, O. S.; Yudilevich, O.; Fassl, P.; Zhou, Q.; Betancur, R.; Munir, R.; Patidar, R.; Stranks, S. D.; Alam, S.; Kar, S.; Unold, T.; Abzieher, T.; Edvinsson, T.; David, T. W.; Paetzold, U. W.; Zia, W.; Fu, W.; Zuo, W.; Schröder, V. R. F.; Tress, W.; Zhang, X.; Chiang, Y. H.; Iqbal, Z.; Xie, Z.; Unger, E. An Open Access Database and Analysis Tool for Perovskite Solar Cells Based on the FAIR Data Principles. *Nat. Energy* **2022**, *7*, 107–115.
- (14) Kim, M.; Jeong, J.; Lu, H.; Lee, T. K.; Eickemeyer, F. T.; Liu, Y.; Choi, I. W.; Choi, S. J.; Jo, Y.; Kim, H. B.; Mo, S. I.; Kim, Y. K.; Lee, H.; An, N. G.; Cho, S.; Tress, W. R.; Zakeeruddin, S. M.; Hagfeldt, A.; Kim, J. Y.; Grätzel, M.; Kim, D. S. Conformal Quantum Dot-SnO₂ Layers as Electron Transporters for Efficient Perovskite Solar Cells. *Science* **2022**, *375*, 302–306.
- (15) Yang, C.; Yin, J.; Li, H.; Almasabi, K.; Gutiérrez-Arzaluz, L.; Gereige, I.; Brédas, J.-L.; Bakr, O. M.; Mohammed, O. F. Engineering Surface Orientations for Efficient and Stable Hybrid Perovskite Single-Crystal Solar Cells. *ACS Energy Lett.* **2022**, *7*, 1544–1552.
- (16) Xiang, W.; Wang, Z.; Kubicki, D. J.; Tress, W.; Luo, J.; Prochowicz, D.; Akin, S.; Emsley, L.; Zhou, J.; Dietler, G.; Grätzel, M.; Hagfeldt, A. Europium-Doped CsPbI₂ Br for Stable and Highly Efficient Inorganic Perovskite Solar Cells. *Joule* **2019**, *3*, 205–214.
- (17) Sheikh, T.; Anilkumar, G. M.; Das, T.; Rahman, A.; Chakraborty, S.; Nag, A. Combining π -Conjugation and Cation– π Interaction for Water-Stable and Photoconductive One-Dimensional Hybrid Lead Bromide. *J. Phys. Chem. Lett.* **2023**, *14*, 1870–1876.
- (18) Bai, F.; Bian, K.; Huang, X.; Wang, Z.; Fan, H. Pressure Induced Nanoparticle Phase Behavior, Property, and Applications. *Chem. Rev.* **2019**, *119*, 7673–7717.
- (19) Pan, Z.; Wu, L.; Jiang, J.; Shen, L.; Yao, K. Searching for High-Quality Halide Perovskite Single Crystals toward X-Ray Detection. *J. Phys. Chem. Lett.* **2022**, *13*, 2851–2861.
- (20) Gui, P.; Chen, Z.; Li, B.; Yao, F.; Zheng, X.; Lin, Q.; Fang, G. High-Performance Photodetectors Based on Single All-Inorganic CsPbBr₃ Perovskite Microwire. *ACS Photonics* **2018**, *5*, 2113–2119.
- (21) Zhang, H.; Nazeeruddin, M. K.; Choy, W. C. H. Perovskite Photovoltaics: The Significant Role of Ligands in Film Formation, Passivation, and Stability. *Adv. Mater.* **2019**, *31*, No. 1805702.
- (22) Balis, N.; Zaky, A. A.; Athanasekou, C.; Silva, A. M.; Sakellis, E.; Vasilopoulou, M.; Stergiopoulos, T.; Kontos, A. G.; Falaras, P. Investigating the Role of Reduced Graphene Oxide as a Universal Additive in Planar Perovskite Solar Cells. *J. Photochem. Photobiol.* **2020**, *386*, 112141.
- (23) Lin, Q.; Armin, A.; Burn, P. L.; Meredith, P. Filterless Narrowband Visible Photodetectors. *Nat. Photonics* **2015**, *9*, 687–694.
- (24) Yao, F.; Gui, P.; Chen, C.; Li, B.; Li, R.; Tao, C.; Lin, Q.; Fang, G. High-Rubidium-Formamidinium-Ratio Perovskites for High-Performance Photodetection with Enhanced Stability. *ACS Appl. Mater. Interfaces* **2019**, *11*, 39875–39881.
- (25) Chao, L.; Xia, Y.; Li, B.; Xing, G.; Chen, Y.; Huang, W. Room-Temperature Molten Salt for Facile Fabrication of Efficient and Stable Perovskite Solar Cells in Ambient Air. *Chem* **2019**, *5*, 995–1006.
- (26) Tran, N. L.; Elkins, M. H.; McMeekin, D. P.; Snaith, H. J.; Scholes, G. D. Observation of Charge Generation via Photo-induced Stark Effect in Mixed-Cation Lead Bromide Perovskite Thin Films. *J. Phys. Chem. Lett.* **2020**, *11*, 10081–10087.
- (27) Ding, J.; Gao, W.; Gao, L.; Lu, K.; Liu, Y.; Sun, J. L.; Yan, Q. Unraveling the Effect of Halogen Ion Substitution on the Noise of Perovskite Single-Crystal Photodetectors. *J. Phys. Chem. Lett.* **2022**, *13*, 7831–7837.
- (28) Shi, D.; Adinolfi, V.; Comin, R.; Yuan, M.; Alarousu, E.; Buin, A.; Chen, Y.; Hoogland, S.; Rothenberger, A.; Katsiev, K.; Losovyj, Y.; Zhang, X.; Dowben, P. A.; Mohammed, O. F.; Sargent, E. H.; Bakr, O. M. Low Trap-State Density and Long Carrier Diffusion in Organolead Trihalide Perovskite Single Crystals. *Science* **2015**, *347*, 519–522.
- (29) Efrati, A.; Aharon, S.; Wierzbowska, M.; Etgar, L. First Evidence of Macroscale Single Crystal Ion Exchange Found in Lead Halide Perovskites. *EcoMat* **2020**, *2*, No. e12016.
- (30) Liu, Y.; Yang, Z.; Cui, D.; Ren, X.; Sun, J.; Liu, X.; Zhang, J.; Wei, Q.; Fan, H.; Yu, F.; Zhang, X.; Zhao, C.; Liu, S. Two-Inch-Sized Perovskite $\text{CH}_3\text{NH}_3\text{PbX}_3$ ($X = \text{Cl}, \text{Br}, \text{I}$) Crystals: Growth and Characterization. *Adv. Mater.* **2015**, *27*, 5176–5183.
- (31) Yao, F.; Peng, J.; Li, R.; Li, W.; Gui, P.; Li, B.; Liu, C.; Tao, C.; Lin, Q.; Fang, G. Room-Temperature Liquid Diffused Separation Induced Crystallization for High-Quality Perovskite Single Crystals. *Nat. Commun.* **2020**, *11*, 1194.
- (32) Almora, O.; Matt, G. J.; These, A.; Kanak, A.; Levchuk, I.; Shrestha, S.; Osset, A.; Brabec, C. J.; Garcia-Belmonte, G. Surface versus Bulk Currents and Ionic Space-Charge Effects in CsPbBr₃ Single Crystals. *J. Phys. Chem. Lett.* **2022**, *13*, 3824–3830.
- (33) Schötz, K.; Askar, A. M.; Peng, W.; Seeberger, D.; Gujar, T. P.; Thelakkat, M.; Köhler, A.; Huettner, S.; Bakr, O. M.; Shankar, K.; Panzer, F. Double Peak Emission in Lead Halide Perovskites by Self-Absorption. *J. Mater. Chem. C* **2020**, *8*, 2289–2300.
- (34) Ng, M.; Halpert, J. E. Single Crystals of Mixed Br/Cl and Sn-Doped Formamidinium Lead Halide Perovskites: Via Inverse Temperature Crystallization. *RSC Adv.* **2020**, *10*, 3832–3836.

- (35) Saidaminov, M. I.; Abdelhady, A. L.; Murali, B.; Alarousu, E.; Burlakov, V. M.; Peng, W.; Dursun, I.; Wang, L.; He, Y.; Maculan, G.; Goriely, A.; Wu, T.; Mohammed, O. F.; Bakr, O. M. High-Quality Bulk Hybrid Perovskite Single Crystals within Minutes by Inverse Temperature Crystallization. *Nat. Commun.* **2015**, *6*, 7586.
- (36) Liu, Y.; Zhang, Y.; Yang, Z.; Feng, J.; Xu, Z.; Li, Q.; Hu, M.; Ye, H.; Zhang, X.; Liu, M.; Zhao, K.; Liu, S. Low-Temperature-Gradient Crystallization for Multi-Inch High-Quality Perovskite Single Crystals for Record Performance Photodetectors. *Mater. Today* **2019**, *22*, 67–75.
- (37) Feng, Y.; Pan, L.; Wei, H.; Liu, Y.; Ni, Z.; Zhao, J.; Rudd, P. N.; Cao, L. R.; Huang, J. Low Defects Density CsPbBr₃ Single Crystals Grown by an Additive Assisted Method for Gamma-Ray Detection. *J. Mater. Chem. C* **2020**, *8*, 11360–11368.
- (38) Mix, L. T.; Ghosh, D.; Tisdale, J.; Lee, M.-C.; O’Neal, K. R.; Sirica, N.; Neukirch, A. J.; Nie, W.; Taylor, A. J.; Prasankumar, R. P.; Tretiak, S.; Yarotski, D. A. Hot Carrier Cooling and Recombination Dynamics of Chlorine-Doped Hybrid Perovskite Single Crystals. *J. Phys. Chem. Lett.* **2020**, *11*, 8430–8436.
- (39) Qiu, L.; Wang, Z.; Luo, S.; Li, C.; Wang, L.; Ke, S.; Shu, L. Perovskite MAPb(Br_{1-x}Cl_x)₃ Single Crystals: Solution Growth and Electrical Properties. *J. Cryst. Growth* **2020**, *549*, 125869.
- (40) Beal, R. E.; Hagström, N. Z.; Barrier, J.; Gold-Parker, A.; Prasanna, R.; Bush, K. A.; Passarello, D.; Schelhas, L. T.; Brüning, K.; Tassone, C. J.; Steinrück, H. G.; McGehee, M. D.; Toney, M. F.; Nogueira, A. F. Structural Origins of Light-Induced Phase Segregation in Organic-Inorganic Halide Perovskite Photovoltaic Materials. *Matter* **2020**, *2*, 207–219.
- (41) Mehdi, H.; Mhamdi, A.; Bouazizi, A. Effect of Perovskite Precursor Ratios and Solvents Volume on the Efficiency of MAPbI_{3-x}Cl_x Mixed Halide Perovskite Solar Cells. *Mater. Sci. Semicond.* **2020**, *109*, 104915.
- (42) Knight, A. J.; Herz, L. M. Preventing Phase Segregation in Mixed-Halide Perovskites: A Perspective. *Energy Environ. Sci.* **2020**, *13*, 2024–2046.
- (43) Ruan, S.; Surmiak, M.-A.; Ruan, Y.; McMeekin, D. P.; Ebendorff-Heidepriem, H.; Cheng, Y.-B.; Lu, J.; McNeill, C. R. Light Induced Degradation in Mixed-Halide Perovskites. *J. Mater. Chem. C* **2019**, *7*, 9326–9334.
- (44) Tang, S.; Chen, J.; Li, C.; Mao, Z.; Cheng, Z.; Zhang, J.; Zhu, M.; Xiang, S.; Zhang, Z. Mixing Halogens Improves the Passivation Effects of Amine Halide on Perovskite. *Electrochim. Acta* **2022**, *405*, 139782.
- (45) Wang, Z.; Zhang, Z.; Xie, L.; Wang, S.; Yang, C.; Fang, C.; Hao, F. Recent Advances and Perspectives of Photostability for Halide Perovskite Solar Cells. *Adv. Opt. Mater.* **2022**, *10* (3), 2101822.
- (46) Billing, D. G.; Lemmerer, A. Synthesis and Crystal Structures of Inorganic-Organic Hybrids Incorporating an Aromatic Amine with a Chiral Functional Group. *CrystEngComm* **2006**, *8* (9), 686–695.
- (47) Maeng, I.; Lee, S.; Tanaka, H.; Yun, J.-H.; Wang, S.; Nakamura, M.; Kwon, Y.-K.; Jung, M.-C. Unique Phonon Modes of a CH₃NH₃PbBr₃ Hybrid Perovskite Film without the Influence of Defect Structures: An Attempt toward a Novel THz-Based Application. *NPG Asia Mater.* **2020**, *12*, 53.
- (48) Xu, J.; Boyd, C. C.; Yu, Z. J.; Palmstrom, A. F.; Witter, D. J.; Larson, B. W.; France, R. M.; Werner, J.; Harvey, S. P.; Wolf, E. J.; Weigand, W.; Manzoor, S.; Van Hest, M. F. A. M.; Berry, J. J.; Luther, J. M.; Holman, Z. C.; McGehee, M. D. Triple-Halide Wide-Band Gap Perovskites with Suppressed Phase Segregation for Efficient Tandems. *Science* **2020**, *367*, 1097–1104.
- (49) Khanam, S. J.; Banerjee, D.; Soma, V. R.; Murali, B. Stability Enhancement and Pronounced Three-Photon Absorption in SrCl₂-Doped FAPbBr₃ Nano Crystals. *J. Mater. Chem. C* **2023**, *11*, 3275–3283.
- (50) Saidaminov, M. I.; Adinolfi, V.; Comin, R.; Abdelhady, A. L.; Peng, W.; Dursun, I.; Yuan, M.; Hoogland, S.; Sargent, E. H.; Bakr, O. M. Planar-Integrated Single-Crystalline Perovskite Photodetectors. *Nat. Commun.* **2015**, *6*, 8724.
- (51) Wang, X.; Li, Y.; Xu, Y.; Pan, Y.; Zhu, C.; Zhu, D.; Wu, Y.; Li, G.; Zhang, Q.; Li, Q.; Zhang, X.; Wu, J.; Chen, J.; Lei, W. Solution-Processed Halide Perovskite Single Crystals with Intrinsic Compositional Gradients for X-Ray Detection. *Chem. Mater.* **2020**, *32*, 4973–4983.
- (52) Zou, Y.; Zou, T.; Zhao, C.; Wang, B.; Xing, J.; Yu, Z.; Cheng, J.; Xin, W.; Yang, J.; Yu, W.; Dong, H.; Guo, C. A Highly Sensitive Single Crystal Perovskite–Graphene Hybrid Vertical Photodetector. *Small* **2020**, *16*, 2000733.
- (53) Wang, Y.; Quintana, X.; Kim, J.; Guan, X.; Hu, L.; Lin, C.-H.; Jones, B. T.; Chen, W.; Wen, X.; Gao, H.; Wu, T. Phase Segregation in Inorganic Mixed-Halide Perovskites: From Phenomena to Mechanisms. *Photonics Res.* **2020**, *8*, A56–71.
- (54) Yamada, Y.; Hoyano, M.; Oto, K.; Kanemitsu, Y. Effects of Impurity Doping on Photoluminescence Properties of APbX₃ Lead Halide Perovskites. *Phys. Status Solidi B* **2019**, *256*, 1800545.
- (55) Zhang, F.; Zhu, K. Additive Engineering for Efficient and Stable Perovskite Solar Cells. *Adv. Ener. Mater.* **2020**, *10*, 1902579.
- (56) Ganeev, R. A.; Rao, K. S.; Yu, Z.; Yu, W.; Yao, C.; Fu, Y.; Zhang, K.; Guo, C. Strong Nonlinear Absorption in Perovskite Films. *Opt. Mater. Express* **2018**, *8*, 1472–1483.
- (57) Jiang, S.; Wang, X.; Wu, Y.; Li, Y. W.; Zhang, Q.; Li, G. W.; Wu, Y.; Zhang, W.; Zhang, X.; Wang, B.; Chen, J.; Lei, W. Balance Lead in Solution-Processed CH₃NH₃PbBr_xCl_(3-x) Single Crystals for High Performance X-Ray Detection. *Mater. Lett.* **2019**, *236*, 26–29.
- (58) Mahapatra, A.; Parikh, N.; Kumari, H.; Pandey, M. K.; Kumar, M.; Prochowicz, D.; Kalam, A.; Tavakoli, M. M.; Yadav, P. Reducing Ion Migration in Methylammonium Lead Tri-Bromide Single Crystal via Lead Sulfate Passivation. *J. Appl. Phys.* **2020**, *127*, 185501.
- (59) Thomson, M. D.; Kreß, M.; Löffler, T.; Roskos, H. G. Broadband THz Emission from Gas Plasmas Induced by Femtosecond Optical Pulses: From Fundamentals to Applications. *Laser Photonics Rev.* **2007**, *1*, 349–368.
- (60) Fedorov, V. Y.; Tzortzakis, S. Powerful Terahertz Waves from Long-Wavelength Infrared Laser Filaments. *Light Sci. Appl.* **2020**, *9*, 186.
- (61) Xie, X.; Dai, J.; Zhang, X.-C. Coherent Control of THz Wave Generation in Ambient Air. *Phys. Rev. Lett.* **2006**, *96*, 075005.
- (62) Cook, D. J.; Hochstrasser, R. M. Intense Terahertz Pulses by Four-Wave Rectification in Air. *Opt. Lett.* **2000**, *25*, 1210–1212.
- (63) Chen, M.-K.; Kim, J. H.; Yang, C.-E.; Yin, S. S.; Hui, R.; Ruffin, P. Terahertz Generation in Multiple Laser-Induced Air Plasmas. *Appl. Phys. Lett.* **2008**, *93*, 231102.
- (64) Ma, D.; Dong, L.; Zhang, R.; Zhang, C.; Zhao, Y.; Zhang, L. Enhancement of Terahertz Wave Emission from Air Plasma Excited by Harmonic Three-Color Laser Fields. *Opt. Commun.* **2021**, *481*, 126533.
- (65) Bera, A.; Bera, S.; Kalimuddin, S.; Gayen, S.; Kundu, M.; Das, B.; Mondal, M. Review of Recent Progress on THz Spectroscopy of Quantum Materials: Superconductors, Magnetic and Topological Materials. *Eur. Phys. J.: Spec.* **2021**, *230*, 4113–4139.
- (66) Heindl, M. B.; Kirkwood, N.; Lauster, T.; Lang, J. A.; Retsch, M.; Mulvaney, P.; Herink, G. Ultrafast Imaging of Terahertz Electric Waveforms Using Quantum Dots. *Light Sci. Appl.* **2022**, *11*, 31–33.
- (67) Roussel, E.; Szwaj, C.; Evain, C.; Steffen, B.; Gerth, C.; Jalali, B.; Bielawski, S. Phase Diversity Electro-optic Sampling: A New Approach to Single-Shot Terahertz Waveform Recording. *Light Sci. Appl.* **2022**, *11*, 14.
- (68) Peng, Y.; Shi, C.; Zhu, Y.; Gu, M.; Zhuang, S. Terahertz Spectroscopy in Biomedical Field: A Review on Signal-to-Noise Ratio Improvement. *Photonix* **2020**, *1*, 12.
- (69) Chen, Z.; Segev, M. Highlighting Photonics: Looking into the next Decade. *eLight* **2021**, *1*, 2.
- (70) Pyne, P.; Das Mahanta, D.; Gohil, H.; Prabhu, S. S.; Mitra, R. K. Correlating Solvation with Conformational Pathways of Proteins in Alcohol-Water Mixtures: A THz Spectroscopic Insight. *Phys. Chem. Chem. Phys.* **2021**, *23*, 17536–17544.
- (71) Sharma, P.; Kumar, M.; Awana, V. P. S.; Singh, A.; Gohil, H.; Prabhu, S. S. Comprehensive Analysis of Terahertz Frequency

- Response of Bi_2Se_3 and Bi_2Te_3 Single Crystals Using Terahertz Time-Domain Spectroscopy. *Mater. Sci. Eng., B* **2021**, *272*, 115355.
- (72) Sindhu, P. S.; Mitra, N.; Ghindani, D.; Prabhu, S. S. Epoxy Resin (DGEBA/TETA) Exposed to Water: A Spectroscopic Investigation to Determine Water-Epoxy Interactions. *J. Infrared, Millimeter, Terahertz Waves* **2021**, *42*, 558–571.
- (73) Neu, J.; Schmuttenmaer, C. A. Tutorial: An Introduction to Terahertz Time Domain Spectroscopy (THz-TDS). *J. Appl. Phys.* **2018**, *124*, 231101.
- (74) Chanana, A.; Liu, X.; Zhang, C.; Vardeny, Z. V.; Nahata, A. Ultrafast Frequency-Agile Terahertz Devices Using Methylammonium Lead Halide Perovskites. *Sci. Adv.* **2018**, *4*, No. eaar7353.
- (75) Sun, Q.; Yang, W.; Cheng, Y.; Dong, J.; Zhu, M.; Zhang, B.; Dubois, A.; Zhu, M.; Jie, W.; Xu, Y. Anisotropic Dielectric Behavior of Layered Perovskite-like $\text{Cs}_3\text{Bi}_2\text{I}_9$ crystals in the Terahertz Region. *Phys. Chem. Chem. Phys.* **2020**, *22*, 24555–24560.
- (76) Zhao, D.; Chia, E. E. M. Free Carrier, Exciton, and Phonon Dynamics in Lead-Halide Perovskites Studied with Ultrafast Terahertz Spectroscopy. *Adv. Opt. Mater.* **2020**, *8*, 1900783.
- (77) Bogue, R. Sensing with Terahertz Radiation: A Review of Recent Progress. *Sensor Rev.* **2018**, *38*, 216–222.
- (78) Yettappu, G. R.; Talukdar, D.; Sarkar, S.; Swarnkar, A.; Nag, A.; Ghosh, P.; Mandal, P. Terahertz Conductivity within Colloidal CsPbBr_3 Perovskite Nanocrystals: Remarkably High Carrier Mobilities and Large Diffusion Lengths. *Nano Lett.* **2016**, *16*, 4838–4848.
- (79) Zhao, D.; Skelton, J. M.; Hu, H.; La-o-vorakiat, C.; Zhu, J.-X.; Marcus, R. A.; Michel-Beyerle, M.-E.; Lam, Y. M.; Walsh, A.; Chia, E. E. M. Low-Frequency Optical Phonon Modes and Carrier Mobility in the Halide Perovskite $\text{CH}_3\text{NH}_3\text{PbBr}_3$ Using Terahertz Time-Domain Spectroscopy. *Appl. Phys. Lett.* **2017**, *111*, 201903.
- (80) Okochi, H.; Katsuki, H.; Tsubouchi, M.; Itakura, R.; Yanagi, H. Photon Energy-Dependent Ultrafast Photo-induced Terahertz Response in a Microcrystalline Film of $\text{CH}_3\text{NH}_3\text{PbBr}_3$. *J. Phys. Chem. Lett.* **2020**, *11*, 6068–6076.
- (81) Ulatowski, A. M.; Herz, L. M.; Johnston, M. B. Terahertz Conductivity Analysis for Highly Doped Thin-Film Semiconductors. *J. Infrared, Millimeter, Terahertz Waves* **2020**, *41*, 1431–1449.
- (82) Xia, C. Q.; Peng, J.; Poncé, S.; Patel, J. B.; Wright, A. D.; Crothers, T. W.; Uller Rothmann, M.; Borchert, J.; Milot, R. L.; Kraus, H.; Lin, Q.; Giustino, F.; Herz, L. M.; Johnston, M. B. Limits to Electrical Mobility in Lead-Halide Perovskite Semiconductors. *J. Phys. Chem. Lett.* **2021**, *12*, 3607–3617.
- (83) Duvillaret, L.; Garet, F.; Coutaz, J.-L. A Reliable Method for Extraction of Material Parameters in Terahertz Time-Domain Spectroscopy. *IEEE J. Sel. Top. Quantum Electron.* **1996**, *2*, 739–746.
- (84) Withayachumankul, W.; Naftaly, M. Fundamentals of Measurement in Terahertz Time-Domain Spectroscopy. *J. Infrared, Millimeter, Terahertz Waves* **2014**, *35*, 610–637.
- (85) Yu, B. L.; Zeng, F.; Xing, Q.; Alfano, R. R. Probing Dielectric Relaxation Properties of Liquid CS_2 with Terahertz Time-Domain Spectroscopy. *Appl. Phys. Lett.* **2003**, *82*, 4633–4635.
- (86) Xia, C. Q.; Poncé, S.; Peng, J.; Ulatowski, A. M.; Patel, J. B.; Wright, A. D.; Milot, R. L.; Kraus, H.; Lin, Q.; Herz, L. M.; Giustino, F.; Johnston, M. B. Ultrafast Photo-Induced Phonon Hardening Due to Pauli Blocking in MAPbI_3 single-Crystal and Polycrystalline Perovskites. *J. Phys. Mater.* **2021**, *4*, 044017.
- (87) Nienhuys, H.-K.; Sundström, V. Intrinsic Complications in the Analysis of Optical-Pump, Terahertz Probe Experiments. *Phys. Rev. B* **2005**, *71*, 235110.
- (88) Lloyd-Hughes, J.; Jeon, T.-I. A Review of the Terahertz Conductivity of Bulk and Nano-Materials. *J. Infrared, Millimeter, Terahertz Waves* **2012**, *33*, 871–925.
- (89) Brivio, F.; Frost, J. M.; Skelton, J. M.; Jackson, A. J.; Weber, O. J.; Weller, M. T.; Goñi, A. R.; Leguy, A. M. A.; Barnes, P. R. F.; Walsh, A. Lattice Dynamics and Vibrational Spectra of the Orthorhombic, Tetragonal, and Cubic Phases of Methylammonium Lead Iodide. *Phys. Rev. B* **2015**, *92*, 144308.
- (90) Sendner, M.; Nayak, P. K.; Egger, D. A.; Beck, S.; Müller, C.; Epding, B.; Kowalsky, W.; Kronik, L.; Snaith, H. J.; Pucci, A.; Lovrinčić, R. Optical Phonons in Methylammonium Lead Halide Perovskites and Implications for Charge Transport. *Mater. Horiz.* **2016**, *3*, 613–620.